Petroleum Science 23 (2026) 1–16

Contents lists available at ScienceDirect

Petroleum Science

journal homepage: www.keaipublishing.com/en/journals/petroleum-science

Original Paper

Shale pore modification induced by syncline bending in the Eastern Fold Belt of Sichuan Basin, South China

Yi-Ting Qiao [a], Rui Liu [a,*], Shang Xu [b,**], Jun-Wei Pu [c], Fang Hao [b], Tong-Tong Luo [d], Ke-Xuan Li [a], Xiu-Cheng Tan [a], Wei-Ming Chen [c], Yu-Feng Tang [a]

[a] School of Geoscience and Technology, Southwest Petroleum University, Chengdu, 610500, Sichuan, China
[b] School of Geosciences, China University of Petroleum (East China), Qingdao, 266580, Shandong, China
[c] Chongqing Shale Gas Exploration and Development Co. Ltd., Chongqing, 401121, China
[d] CCDC Geological Exploration & Development Research Institute, Chengdu, 610056, Sichuan, China

ARTICLE INFO

Article history:
Received 16 April 2025
Received in revised form
2 July 2025
Accepted 2 September 2025
Available online 4 September 2025

Edited by Jie Hao and Xi Zhang

Keywords:
Syncline bending
Pore structure
Porosity reduction
Detachment fold
Organic-rich shale
Tectonic stress

ABSTRACT

Shale deformation is crucial in various geological processes. To investigate the effect of deformation on pore characteristics for highly compacted shale, the macro tectonic strain and micro pore structure were analyzed in the deeply buried Wufeng–Longmaxi shale of the Eastern Fold Belt of the Sichuan Basin. Despite similarities in their X-ray diffraction mineral compositions, significant differences in pore properties were observed between the shale samples from weak and strong curved synclines. Pore shapes identified from scanning electron microscopy and the covariation between total organic carbon (TOC) content and porosity suggest that organic pores predominantly contribute to total porosity. However, samples from weak-curved synclines exhibit porosities ~2% higher than samples from strong-curved synclines, even with similar TOC contents. Compared to the weak-curved syncline samples, the strong-curved syncline samples show a transformation in organic pore morphology from spherical to elliptical with an increasing aspect ratio and reduced dominant pore size from 1–1000 nm to 1–100 nm due to pore collapse in the organic matrix. The porosities simulated using a syncline bending ductile strain model align well with the measured porosities, indicating that the porosity changes were induced by heterogeneous ductile strain during detachment folding. Strain heterogeneity also triggered tectonic stress heterogeneity, causing clockwise rotation of the principal stress orientation from weak to strong curved synclines. This study improves our understanding of the variations in pore system with syncline deformation strain, providing a theoretical basis for subsequent shale hydrocarbon exploration and resource assessment in complex tectonic zones.

1. Introduction

Despite the high abundance [75% of the sedimentary rocks (Olgaard et al., 1995)] of shale in the Earth's crust, the progressive distortion of shale pores was, until recently, a relatively neglected aspect of shale deformation, and many questions remain unanswered. Pores in shale can vary through time because of their ductile deformation. In the upper crust, ductile shale deformation often occurs as burial compaction, involving pore morphology or size alteration during the rotation and alignment of competent particles and distortion of incompetent material (e.g., organic matter and certain clay minerals) (Aplin and Macquaker, 2011; Athy, 1930; Dewhurst et al., 1998). The long axis of matrix particles is subparallel to the bedding owing to the predominance of vertical shortening during burial compaction; however, in areas of lateral tectonic shortening, such as the early stage of shale-dominated detachment deformation (Laurich et al., 2014; Moore et al., 2011; Morley and Naghadeh, 2018; Saito and Goldberg, 2001; Screaton et al., 2002), the angle of particle long axis to the bedding is high. Despite the considerable variation in degree of pore adjustment to the textural and mineral composition of shale (Mondol et al., 2007), the prevailing hypothesis is that porosity loss from ductile shale deformation is predominant at burial depths of <2 km, considering the subsequent inhabitation by

---

[*] Corresponding author.
[**] Corresponding author.
E-mail addresses: liurui@outlook.com (R. Liu), xushang@upc.edu.cn (S. Xu).
Peer review under the responsibility of China University of Petroleum (Beijing).

https://doi.org/10.1016/j.petsci.2025.09.002

chemical cementation and overpressure generation at greater burial depths (Bjørlykke, 2014).

However, recent analysis of deeply buried shale cores has revealed impressive pore alteration during ductile shale deformation (Guo et al., 2022; Liu et al., 2020a; Wang, 2020). The laboratory compression of gas/oil-rich shale cores [e.g., Wufeng–Longmaxi shale (Cheng et al., 2024; Li et al., 2024) and Alum Shale (Sone et al., 2015)] directly displayed heterogeneous ductile deformation, where organic matter and macropores exhibit a higher degree of compliance than inorganic minerals and micropores, respectively. Furthermore, in tectonically deformed gas shale, such as fault gouges (Zhu et al., 2018), folds (Guo et al., 2022; Li et al., 2021a; Liu et al., 2020a, 2020b; Ma et al., 2020; Shi et al., 2021; Yang et al., 2022), and detachment horizons (Liang et al., 2017), variations in pore parameters (e.g., morphology, size, and volume) are increasingly reported. Nevertheless, the model of shale pore variation during tectonic deformation remains controversial, potentially because of the superposition of ductile and brittle deformations. This is particularly true for outcrop studies (Zhu et al., 2018).

Core samples drilled from commercial shale gas boreholes located far from fault damage zone and uplift denudation area have shown a more pronounced correlation between pore parameters and ductile deformation strain (Gou et al., 2021; Guo et al., 2022; Liu et al., 2020a, 2020b; Yang et al., 2022). However, most core analyses have focused on samples from detachment anticlines, comparing pores sizes and shapes in open and closed anticlines (Liu et al., 2020a; Yang et al., 2022), between the limb and core of the anticline, and between the forelimb and backlimb of the basement-involved anticline (Liu et al., 2020b). These

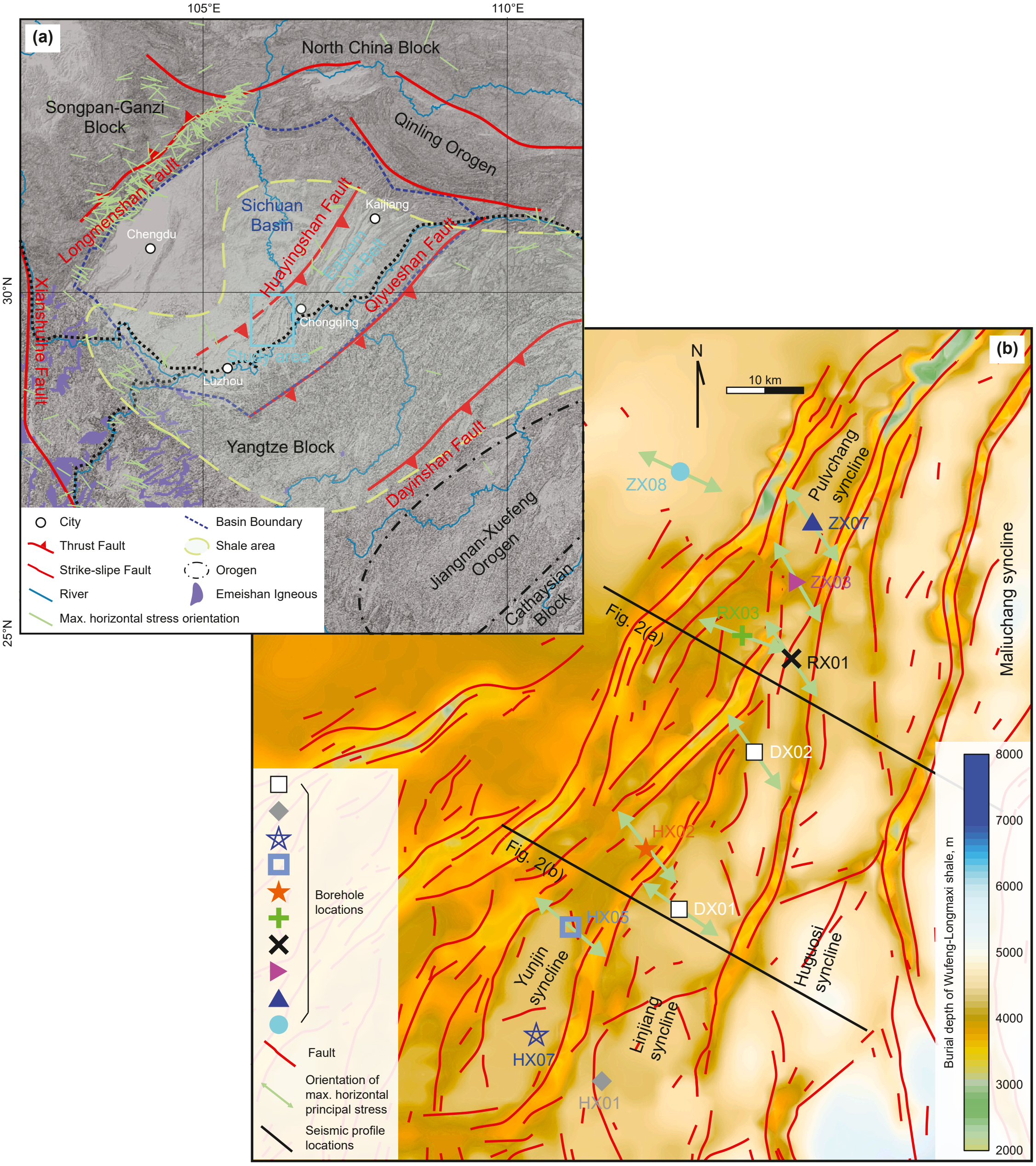

Fig. 1. **(a)** Tectonic settings of the Sichuan Basin, with maximum horizontal stress orientation derived from (Heidbach et al., 2018). **(b)** Fault system and burial depth of the Wufeng–Longmaxi shale in the study area, with maximum horizontal stress orientation obtained from an internal report based on the Formation MicroScanner Image log.

studies have attributed the spatial variation in shale porosity to the ductile bending strain of gas-rich shale during the kinematic growth of detachment folding with high amplitude-wavelength ratios (>0.2). Notably, the downward deflection of synclines is flatter and has lower amplitudes compared to the upward deflection of anticlines during detachment folding (Mitra, 2003), and the potential effects of the weak deformation strain of detachment synclines with low amplitude-wavelength ratios (<0.1) to the shale pore system warrants further investigation.

To improve our understanding of the internal connection between detachment syncline deformation and shale pore evolution, this study integrated fold curvature quantification with core analyses to compare the matrix composition, pore parameters (morphology, size, and volume), and ductile bending strain in the Paleozoic Wufeng-Longmaxi shale from various detachment synclines in the Eastern Fold Belt of the Sichuan Basin, South China (Fig. 1).

2. Geological setting

The study area is located in the Paleozoic Wufeng-Longmaxi shale in the Sichuan Basin because it has been identified as the optimal field laboratory for shale deformation studies because of the occurrence of diverse tectonic folding strains within the same shale horizon. The Sichuan Basin, bounded by fold-thrust belts, has a rhomboid outline in the western Yangtze Block (Fig. 1(a)). The Early Paleozoic convergence between the Cathaysia and Yangtze blocks resulted in the transition from a carbonate platform to the semi-restricted Yangtze Sea, where the high primary productivity and anoxic watermass promoted the deposition of the organic-rich Wufeng-Longmaxi black shales (Fig. 2(a)) (Zou et al., 2018; Ran et al., 2025). The Cathaysian–Yangtze convergence during the Jurassic–Cretaceous period compressed and folded Paleozoic–Lower Mesozoic strata (Fig. 2(b)), including the Wufeng–Longmaxi shale, from southeast to northwest. This resulted in forming a large-scale NE–SW-striking fold-thrust belt in the eastern Sichuan Basin, termed the Eastern Sichuan Fold (or Fold-Thrust) Belt. The Huayingshan Fault in the Sichuan Basin marks the western boundary of this belt (Li et al., 2021b; Yan et al., 2003; Gao et al., 2025). The collision between the Songpan–Ganzi and Yangtze blocks during the Cenozoic (driven by the uplift of the Tibetan Plateau) is suspected to have caused the counterclockwise rotation of the Sichuan Basin, which deflected the NE–SW-striking fold-thrust belt and generated the en-echelon folding along the southern Huayingshan Fault (Li et al., 2020; Tong et al., 2018; Wang et al., 2014).

The study area is in the en-echelon fold belt of the southern Huayingshan Fault Zone (Fig. 1(b)). Seismic reflection profiles from this area display typical characteristics of detachment folds, with parallel fold geometries above the Cambrian strata (Fig. 2). The Cambrian strata in the Sichuan Basin are widely considered to be

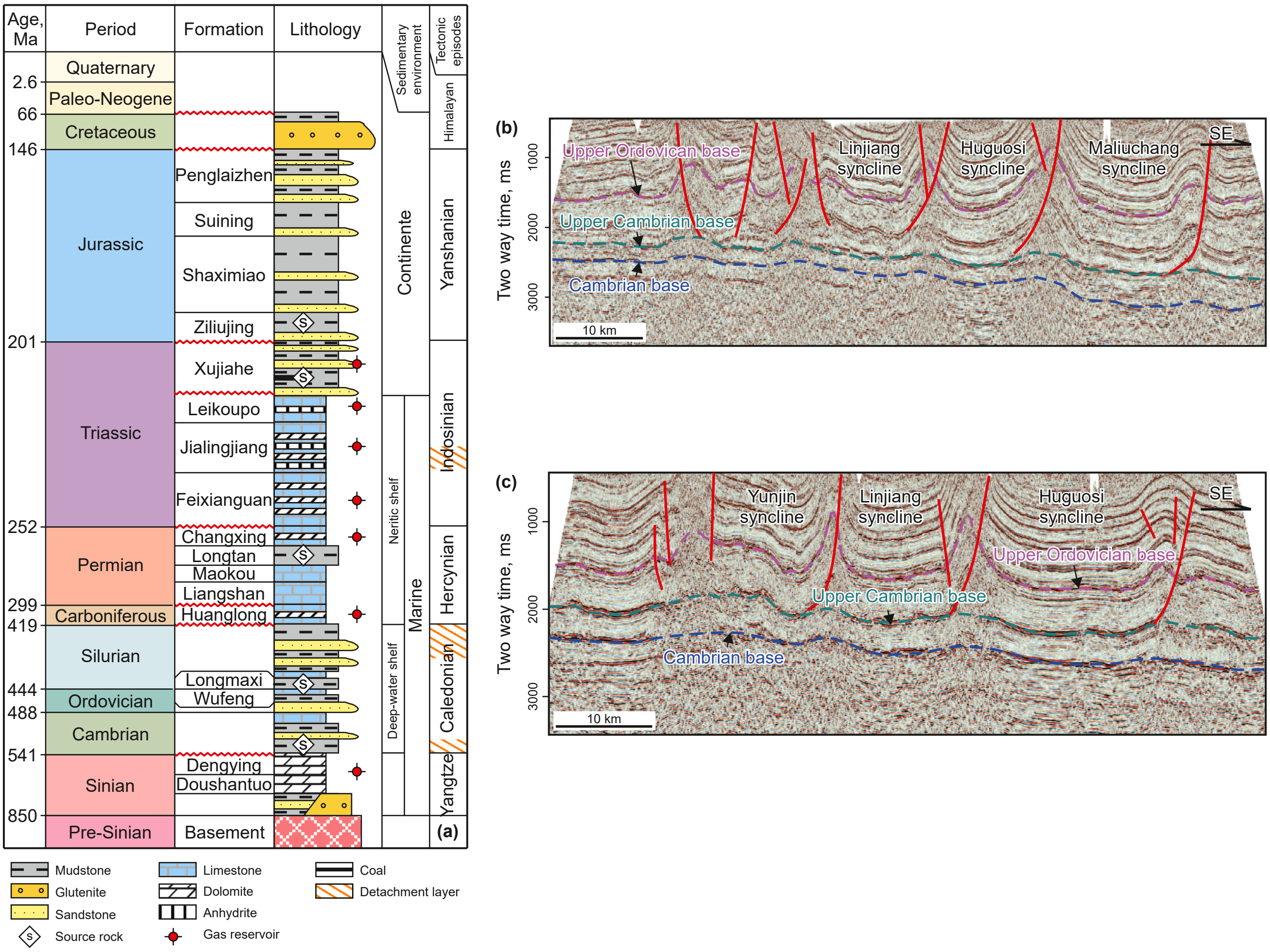

Fig. 2. (**a**) Stratigraphic column of Sichuan Basin derived from seismic profiles illustrating the detachment fold structures north (**b**) and south (**c**) of the study area.

the detachment basal layer owing to the presence of gypsum-bearing layers, such as the Longwangmiao and Gaotaizi Formations (Li et al., 2021b; Liu et al., 2021a). The initial shortening of the layers above the Cambrian gypsum layers resulted in the upward and downward deflection of the anticline and syncline, respectively. The downward synclinal deflection promoted the migration of gypsum units from the synclinal area into the anticline core; and limb lengthening and rotation ultimately led to the tightening and increased amplitude of the anticlines (Brandes and Tanner, 2014; Mitra, 2003). Consequently, the anticlines have undergone more intense deformation and exhibited more brittle faulting than the synclines; thus, the synclines may provide valuable information regarding ductile deformation. The present maximum horizontal stress orientations in the study area, as revealed by the induced tensile hydraulic fractures and borehole breakouts of the Wufeng-Longmaxi shale, are predominantly oriented 115°–150° E (Fig. 1(b), Table 1), which roughly agrees with the regional stress field driven by the southeastern extrusion of the Tibetan plateau (Fig. 1(a)) (Heidbach et al., 2018).

3. Methodology

3.1. Fold curvature analyses

Curvatures were calculated using the method of Bergbauer and Pollard (2003), which characterizes curved surfaces through tangent and normal vectors at each point. Normal curvature at a point reflects the curvature of an arbitrary surface curve in a given direction, reaching minimum and maximum values in two orthogonal directions, i.e., the principal curvatures of K_{min} and K_{max}, respectively (with negative and positive values for syncline and anticline, respectively). The mean (K_{mean}) and Gaussian (K_{gaussian}) curvatures are calculated by (Roberts, 2001):

$$K_{\text{mean}} = 0.5 \times (K_{\text{max}} + K_{\text{min}}) \tag{1}$$

$$K_{\text{gaussian}} = K_{\text{max}} \times K_{\text{min}} \tag{2}$$

3.2. Shale core analyses

Core plugs of the Wufeng–Longmaxi shale, with a sampling interval of ~1 m (avoiding visible cracks), were obtained from nine boreholes at burial depths of 4050–4380 m. These boreholes were selected for spatial comparison between different synclines or between different positions of the same syncline. (Fig. 1(b), Table 1).

For porosity measurements, core plugs with heights and diameters of 3–5 cm and 2–2.5 cm, respectively, were subjected to a drying process at 60 °C until a constant weight was achieved to remove residual fluids. Porosity measurements, based on Archimedes' principle and Boyle's gas law, were conducted using a KXD-II porometer with helium gas (Allshorn et al., 2019; Luffel and Howard, 1988).

The pore sizes of the core plugs were determined via low-field nuclear magnetic resonance (NMR) using a MicroMR23-060H-1 instrument. The pore size (diameter, d in μm) was estimated by Liu et al. (2018):

$$d/2 = F_s \rho_2 T_2 \tag{3}$$

where the T_2 spectrum was obtained at 32 °C with a frequency of 22 MHz and a magnetic field strength of 0.3 T, F_s denotes the pore shape factor, which can be assumed to be three and two for spherical and cylindrical pores, respectively, and ρ_2 denotes the surface relaxivity.

The crushed core samples (1 g) were chemically treated with 5% HCl (12 h) to exclude the effect of inorganic carbon (carbonate), and total organic carbon (TOC) content was determined by combustion in a LECO CS-200 elemental analyzer. The bulk mineralogy of the powdered samples (~100 mesh) was determined using a Bruker D8 X-ray diffractometer with Cu–Ka radiation. Stepped scanning measurements were performed between 10° and 80° (2θ) on random mounts at a scan rate of 4°/min, with the X-ray source operating at an accelerating voltage of 40 kV and a current of 30 mA. The X-ray diffraction (XRD) patterns were interpreted using HighScore Plus software (Degen et al., 2014).

A Zeiss Sigma 300 scanning electron microscope (SEM) operating at 5–15 kV with a 5–16.5 mm working distance was used to image the unpolished and polished surfaces of core fragments. The polished surfaces of the rock fragments were ion-milled utilizing a broad argon ion beam.

4. Results

4.1. Syncline curvature characteristics

The curvature parameters on the top of the Wufeng–Longmaxi shale are illustrated in Fig. 3. The data show a positive correlation between absolute K_{max} and K_{min} values (i.e., $|K_{\text{max}}|$ and $|K_{\text{min}}|$), with the lowest $|K_{\text{max}}|$ and $|K_{\text{min}}|$ values observed in borehole ZX08 and

Table 1
Sampling, measurement, and observation strategies.

Borehole	Syncline	Maximum horizontal stress orientation[a], °	K_{max}, $\times 10^{-5}$ m^{-1}	K_{mean}, $\times 10^{-4}$ m^{-1}	K_{min}, $\times 10^{-4}$ m^{-1}	K_{gaussian}, $\times 10^{-9}$ m^{-2}	Number of samples					Mean porosity, %
							XRD	TOC	Porosity	SEM	NMR	
ZX08	n.d.	115	0.10	−0.06	−0.13	−0.01	33	33	33	10	4	6.44
ZX07	Pulvchang	144	−2.97	−0.68	−1.07	3.17	59	59	59	10	6	3.96
ZX03	Pulvchang	149	−3.33	−0.85	−1.37	4.56	50	57	57	10	n.d.	4.03
HX02	Yujin	141	−1.14	−0.71	−1.30	1.47	63	36	64	n.d.	n.d.	4.05
HX05	Yujin	132	−0.02	−0.37	−0.75	0.01	64	65	65	n.d.	n.d.	6.47
HX07	Yujin	n.d.	−1.50	−0.29	−0.43	0.64	56	56	56	n.d.	n.d.	6.06
RX03	n.d.	111	−2.92	−0.40	−0.52	1.51	74	42	74	n.d.	n.d.	5.22
RX01	Linjiang	146	−5.23	−1.46	−2.39	12.48	51	51	51	n.d.	n.d.	3.57
HX01	Linjiang	n.d.	−1.26	−0.37	−0.61	0.77	70	42	70	n.d.	n.d.	5.62
DX01	Linjiang	124	−2.32	−0.50	−0.77	1.77	n.d.	n.d.	n.d.	n.d.	n.d.	n.d
DX02	Linjiang	145	−2.96	−0.73	−1.17	3.47	n.d.	n.d.	n.d.	n.d.	n.d.	n.d

[a] Indicates data obtained from the Formation MicroScanner Image log report from drilling-induced tensile fracture and borehole breakout strikes; XRD = X-ray diffraction; TOC = total organic carbon; SEM = scanning electron microscopy; NMR = nuclear magnetic resonance; n.d. = no data available.

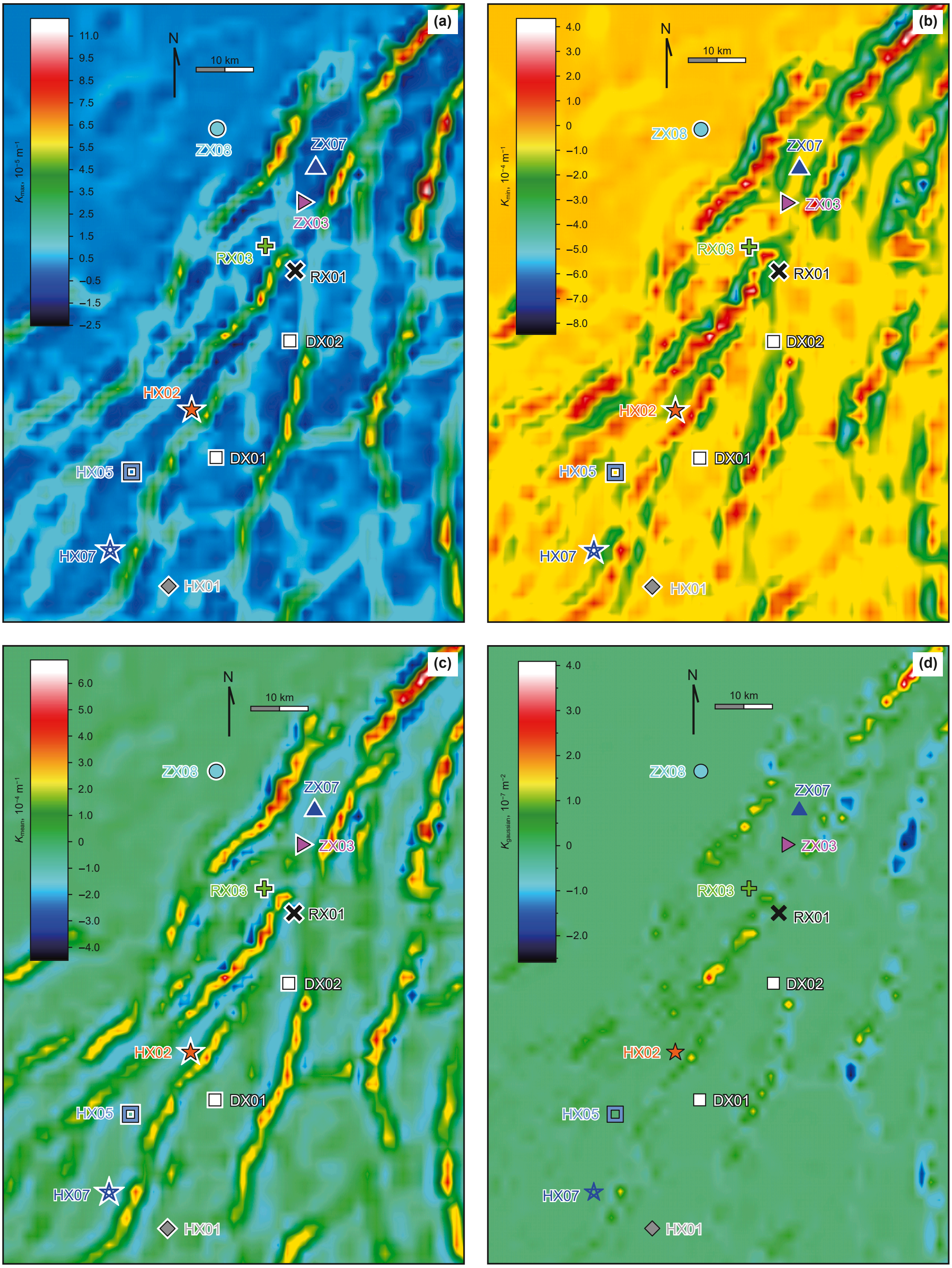

Fig. 3. **(a)** Maximum (K_{max}), **(b)** minimum (K_{min}), **(c)** mean (K_{mean}), and **(d)** gaussian ($K_{gaussian}$) curvatures of the Wufeng-Longmaxi shale in the study area.

the highest $|K_{\text{max}}|$ and $|K_{\text{min}}|$values in borehole RX01 (Fig. 4(a)). Similarly, positive relationships are observed between absolute K_{mean} and K_{gaussian} values (i.e., $|K_{\text{mean}}|$ and $|K_{\text{gaussian}}|$) (Fig. 4(b)). Borehole RX01 has the highest $|K_{\text{gaussian}}|$ value, and borehole ZX08 has the lowest $|K_{\text{gaussian}}|$ value. Additionally, curvature extent decreases with decreasing amplitude-wavelength ratio within the same syncline structure. For example, $|K_{\text{gaussian}}|$ is higher in borehole ZX03 than in borehole ZX07 in the Pulvchang syncline; $|K_{\text{gaussian}}|$ decreases from borehole HX02 to boreholes HX05 and HX07 in the Yunjin syncline; and $|K_{\text{gaussian}}|$ decreases from borehole RX01 to boreholes DX02, DX01, and HX01 in the Linjiang syncline.

To evaluate the influence of curvature on the shale pore system, the nine sampling boreholes were classified into three syncline-based groups (Table 1). To enable comparison of extreme curvature parameters with nearby structural zones, borehole ZX08 (west of the Pulvchang syncline) was assigned to the Pulvchang group, and borehole RX03 (northwest of the Linjiang syncline) was assigned to the Linjiang group.

4.2. Shale matrix characteristics

Despite the vertical variation in mineral compositions caused by sea level fluctuations (Chen et al., 2021) (Fig. 5(a) and (b)), XRD mineralogy reveals that most samples have a dominant quartz composition (40%–80%), followed by clay (20%–60%) and carbonate minerals (0–40%) (Fig. 6). Various amounts of feldspar and pyrite were also observed (Fig. 5(a) and (b)). SEM observations confirm the presence of various mineral particles, predominantly quartz, carbonate minerals, and clay minerals (Fig. 7(a)–(c)). Clay mineral plates exhibit a strong preferred alignment.

Vertically, the TOC content was the highest at the boundary between the Wufeng and Longmaxi formations in each borehole (Fig. 5(a) and (b)), which can be attributed to the sea level fluctuations. Nevertheless, the TOC content varies from 0 to 6% across all boreholes (Fig. 8(a)–(c)). In the SEM images, organic matter is disseminated throughout the samples (Fig. 7 (d)).

4.3. Shale pore characteristics

The porosity measured using a helium pycnometer primarily ranges from 1% to 8%, with an average of 5.31% for all samples (Fig. 8). A positive correlation was observed between porosity and TOC content across all boreholes (Fig. 8(a)–(c)), with an average fit line of $Y = 0.47X + 3.86$ for all samples. Lateral variations in porosity within the same syncline are shown in TOC-porosity plots. Samples from boreholes HX01 and RX01 plot above and below the average line of $Y = 0.47X + 3.86$ in the Linjiang syncline, respectively (Fig. 6(b)); similarly, in the Yunjin synclines, HX07/HX05 samples exceed the average line, whereas HX02 samples lie below it (Fig. 6(c)). The mean porosity correlates with curvature parameters for the nine boreholes (Fig. 9). At comparable TOC levels, samples from boreholes with high $|K_{\text{gaussian}}|$ (or $|K_{\text{max}}|$, $|K_{\text{min}}|$, $|K_{\text{mean}}|$) display ~2% higher porosity than those with low $|K_{\text{gaussian}}|$ (or $|K_{\text{max}}|$, $|K_{\text{min}}|$, $|K_{\text{mean}}|$) within the same syncline (Figs. 8(d)–(f), 9(c) and (d)). The ZX08 samples, which have the lowest $|K_{\text{mean}}|$, show a higher mean porosity (6.44%) compared to the samples obtained from boreholes ZX07 (3.96%) and ZX03 (4.03%) within the nearby Pulvchang syncline. Conversely, the RX01 samples, which exhibit the highest $|K_{\text{mean}}|$, show a lower mean porosity (3.57%) relative to the samples from nearby RX03 (5.22%) in a different syncline.

Various pore types were identified in the SEM images, including pores within the organic matter (i.e., organic pores), intraparticle pores within the detrital carbonate grains, and interparticle pores between the detrital clay plates or authigenic pyrite grains. Organic pores are more prevalent than the mineral-associated intra-/interparticle pores in the SEM images (Fig. 10). Samples obtained from boreholes ZX07/ZX03, which have mean porosities below the average of 5.31% across the nine boreholes, show abundant organic pores with an ellipsoidal or elongated morphology and a high aspect ratio (Fig. 10(a)–(c)). In contrast, organic pores in ZX08 samples, which have a mean porosity exceeding 5.31%, commonly exhibit a sponge-like, spherical morphology (Fig. 10(d)–(f)).

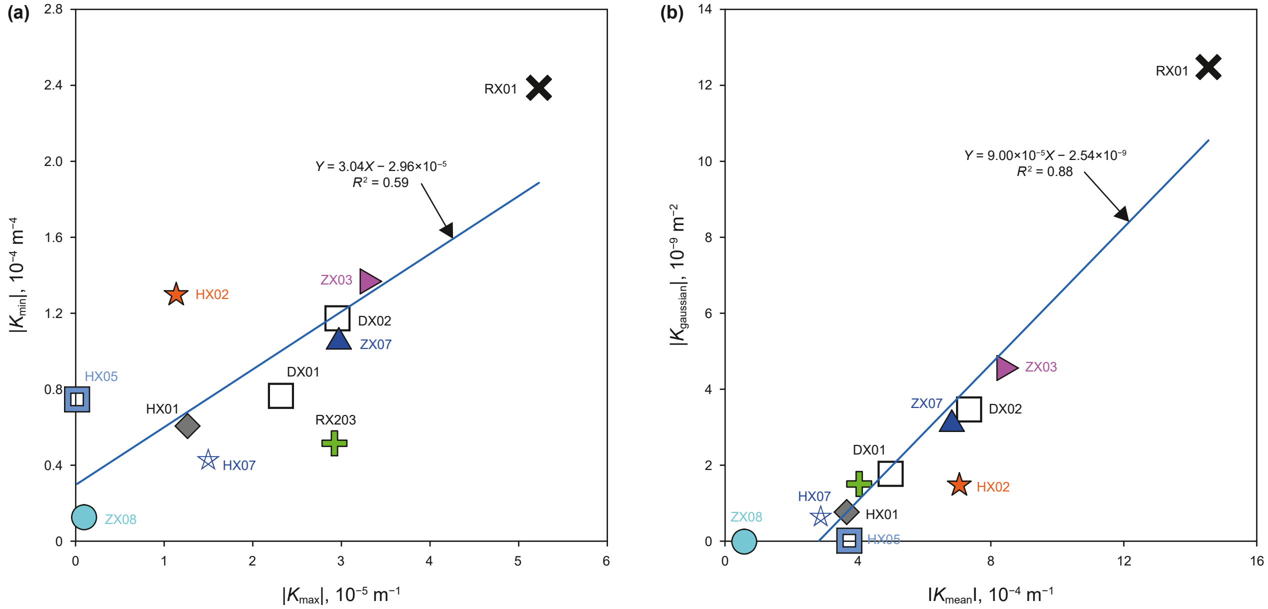

Fig. 4. **(a)** Absolute value of the maximum curvature ($|K_{\text{max}}|$) plotted against the absolute value of the minimum curvature ($|K_{\text{min}}|$). **(b)** Absolute value of the mean curvature ($|K_{\text{mean}}|$) plotted against the absolute value of the Gaussian curvature ($|K_{\text{gaussian}}|$).

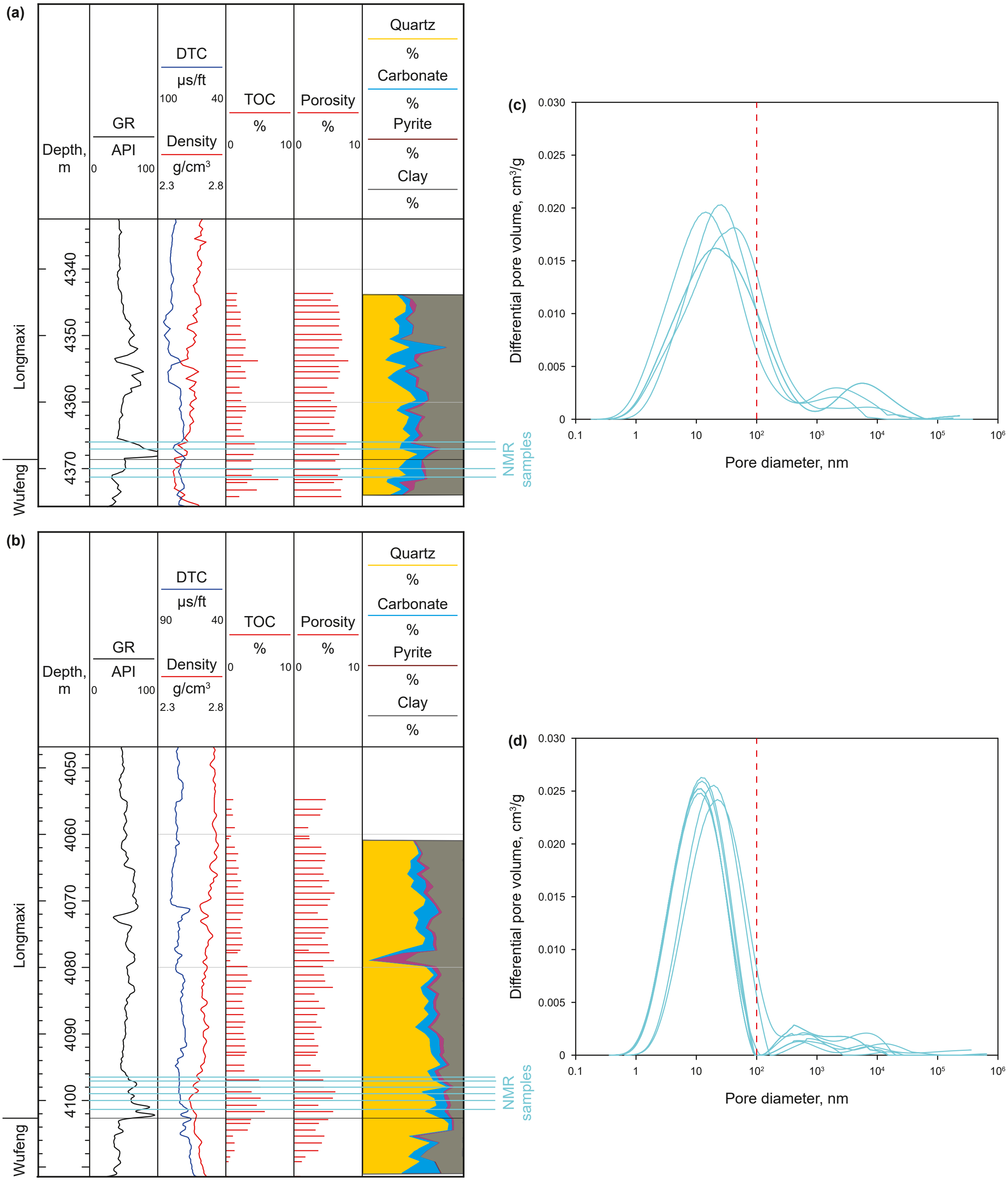

Fig. 5. Vertical variations in total organic carbon (TOC), porosity, and mineral compositions measured from Wufeng–Longmaxi shale core samples in boreholes **(a)** ZX08 and **(b)** ZX03. Pore sizes determined by nuclear magnetic resonance (NMR) for samples obtained from boreholes **(c)** ZX08 and **(d)** ZX03 are shown. Sample locations are indicated in Fig. 3(a) and (b).

The pore size distribution determined by the NMR technique varies significantly between the boreholes, with mean porosities above and below the 5.31% average. Pore size primarily ranges from 1 to 1000 nm and from 1 to 100 nm in samples from boreholes ZX08 (with mean porosity of 6.44%) and ZX03 (with mean porosity of 4.03%), respectively (Fig. 5(c) and (d)), demonstrating more macropores (>50 nm) in the high porosity samples obtained from low $|K_{\mathrm{gaussian}}|$ (or $|K_{\max}|$, $|K_{\min}|$, $|K_{\mathrm{mean}}|$) borehole. Pore sizes >1000 nm, potentially caused by microfractures, were also identified in samples from boreholes ZX03 and ZX08 (Fig. 5(c) and (d)).

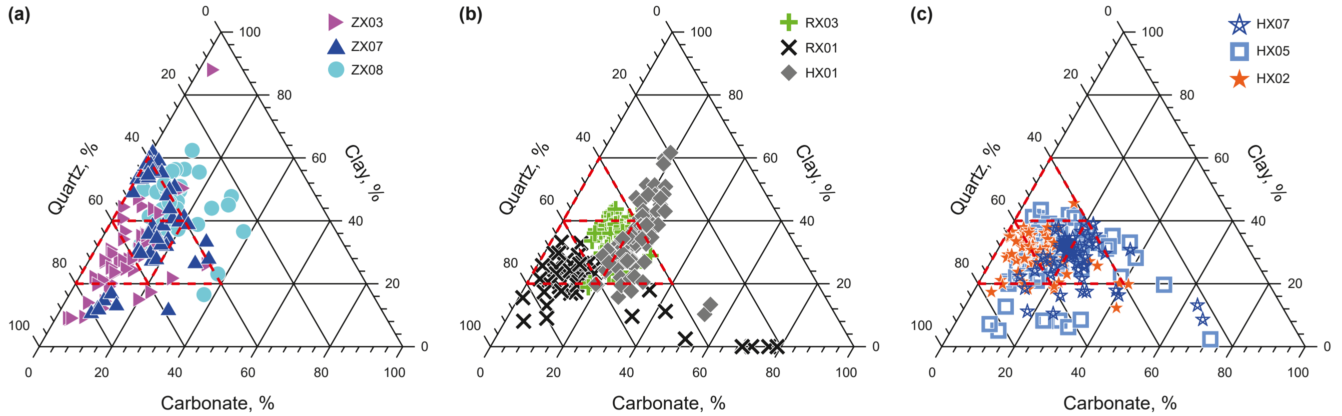

Fig. 6. X-ray diffraction (XRD) mineralogical composition of the Wufeng–Longmaxi shale for different boreholes. **(a)** Boreholes ZX08 and ZX03/ZX07. Boreholes ZX03 and ZX07 are located in the Pulvchang syncline, and nearby borehole ZX08 is situated to the west of the Pulvchang syncline area. **(b)** Boreholes RX03, RX01, and HX01 in the Linjiang syncline. **(c)** Boreholes HX07, HX05, and HX02 in the Yunlin syncline.

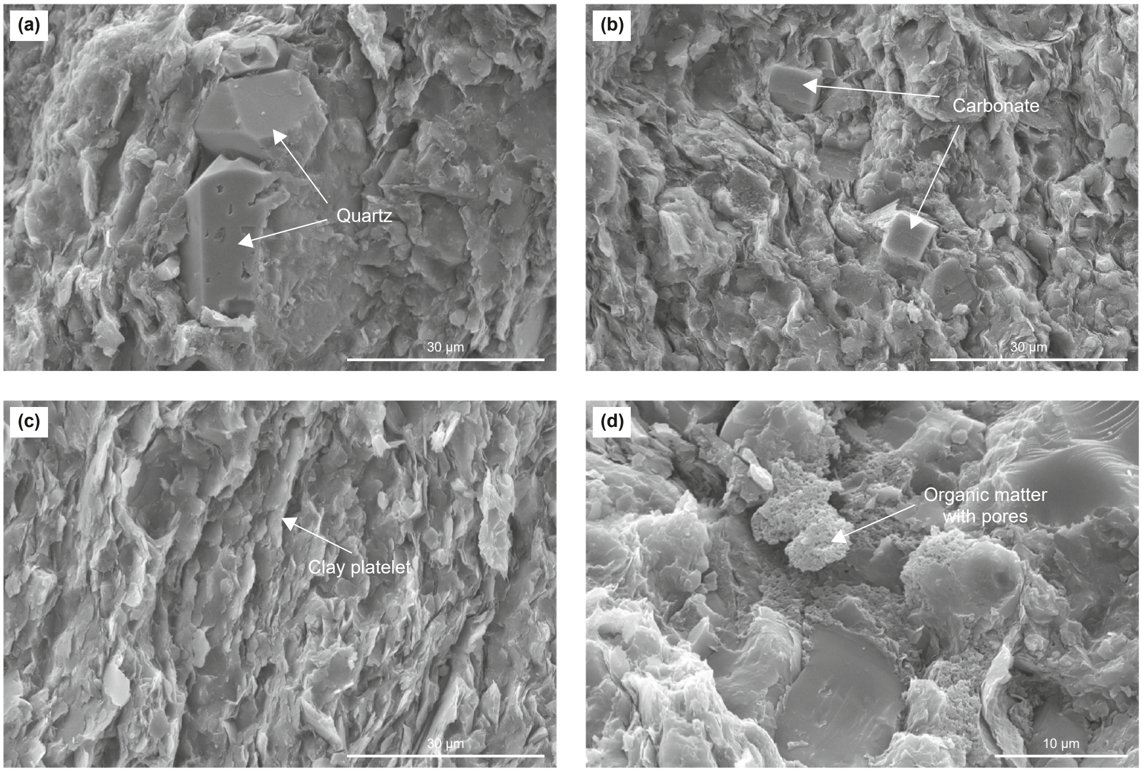

Fig. 7. Photomicrographs showing the matrix characteristics of the Wufeng–Longmaxi shale in the study area: The inorganic detrital minerals of **(a)** quartz, **(b)** carbonate, **(c)** clay platelet, and **(d)** organic matter.

5. Discussion

5.1. *Mechanisms driving lateral porosity variation*

The positive relationship between TOC content and porosity (Fig. 8(a)–(c)), along with SEM observations (Fig. 10), suggests that in the study area the pore system in the Wufeng–Longmaxi shale is primarily composed of organic pore; this is consistent with previous interpretations of porosity in the Wufeng–Longmaxi shale (Guo et al., 2022; Hu et al., 2017; Liu et al., 2020b).

Shale pores in organic material can originate either as primary pores inherited from the organic structure or as secondary pores formed through the thermal maturation of organic matter (Lohr et al., 2015). Therefore, the composition and thermal maturity of organic matter are crucial factors that can result in variations in organic pore generation in certain shales (Curtis et al., 2012; Han et al., 2017; Ko et al., 2018; Mastalerz et al., 2013). Despite porous and non-porous organic particles being widely reported in the same SEM image, the degree of bulk porosity variation attributable to these differences is not always clearly reported (Curtis et al., 2012). Regarding the role of thermal maturity, significant porosity fluctuation (>5%) has been observed to primarily occur within the vitrinite reflectance range of 0.5%–1.5%, which corresponds to the liquid generation and cracking stage (Han et al., 2017; Ko et al., 2018; Mastalerz et al., 2013). In the study area, the lateral variation in the depositional setting of the

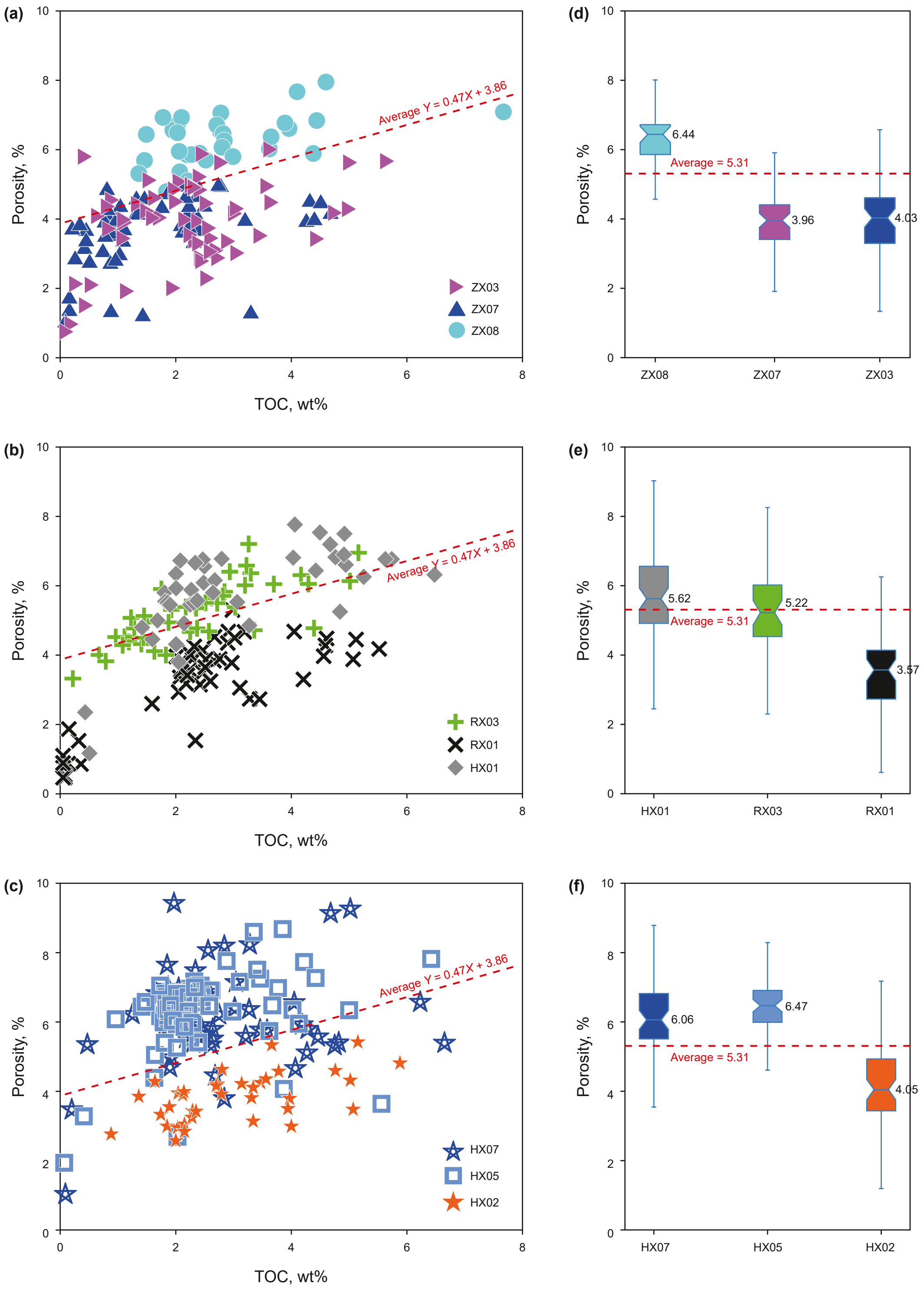

Fig. 8. TOC content and porosity measured from samples in the various synclines. **(a)** Boreholes ZX08 and ZX03/ZX07. **(b)** Boreholes RX03, RX01, and HX01. **(c)** Boreholes HX07, HX05, and HX02.

Wufeng–Longmaxi shale is minimal and can be disregarded (Lu et al., 2020).The Wufeng–Longmaxi shale exhibits lateral homogeneity in its inorganic and organic compositions, with dominant mineral contents of 40%–80% quartz, 20%–60% clay, and 0–40% carbonate (Fig. 6), along with a general TOC content of 0–6% (Fig. 8(a)–(c)). Furthermore, the thermal maturity of the Wufeng–Longmaxi shale is nearly constant at 2.4%–2.5% vitrinite reflectance (Feng et al., 2018). Considering the similarities in matrix components and thermal maturity levels across the different boreholes, the lateral variation in porosity is unlikely to be primarily driven by differences in organic pore generation (Fig. 8(d)–(f)). Other factors, particularly pore preservation, may play a more significant role in controlling the observed porosity heterogeneity.

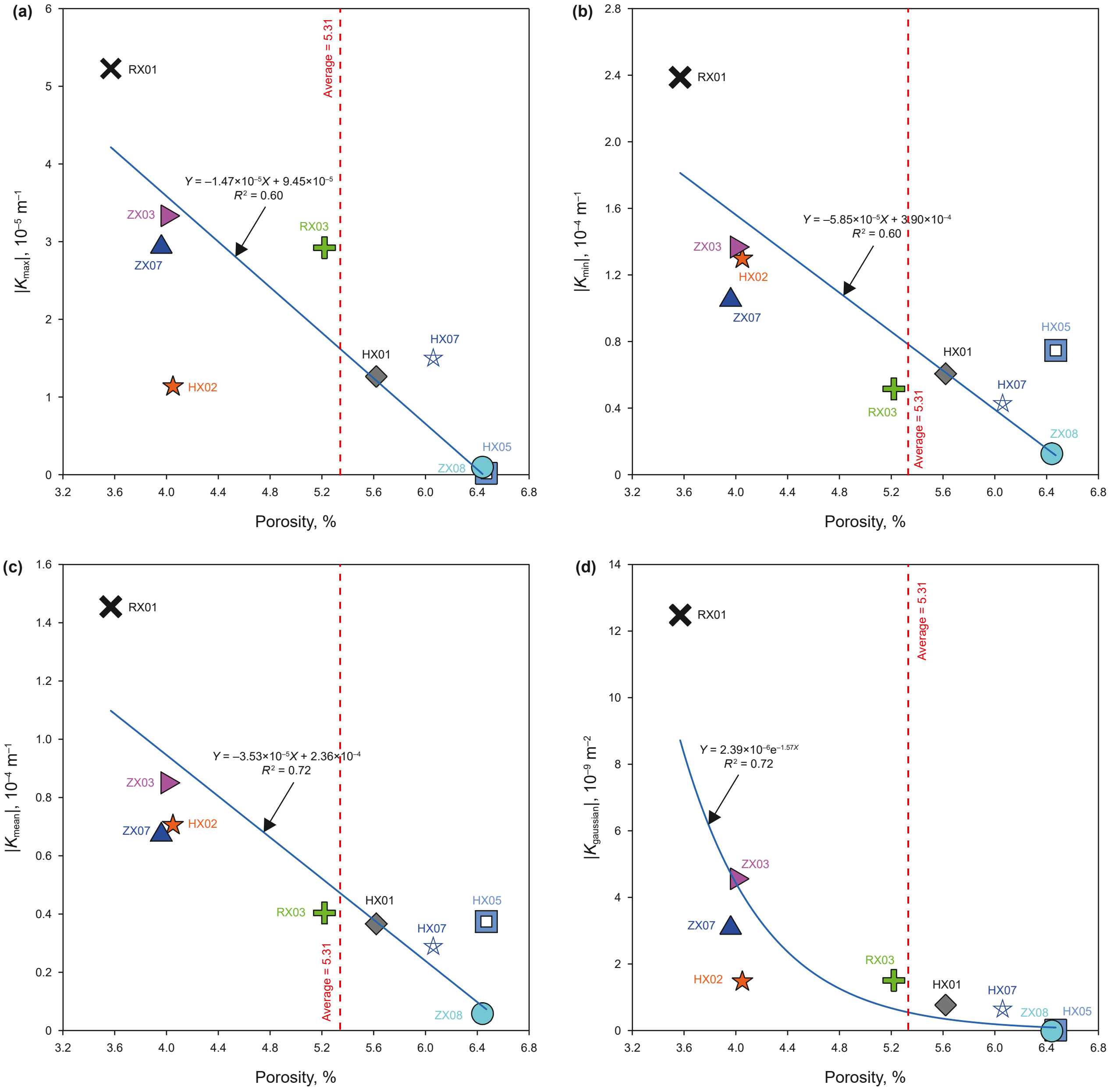

Fig. 9. Cross-plots of the absolute values of various curvature attributes, including **(a)** $|K_{\max}|$, **(b)** $|K_{\min}|$, **(c)** $|K_{\text{mean}}|$, and **(d)** $|K_{\text{gaussian}}|$, with mean porosity in the Wufeng-Longmaxi shale of various boreholes in the study area.

Notably, the organic pores can be mechanically deformed after their generation. Organic matter has a lower Young's modulus (approximately 5–10 GPa) than inorganic minerals (Eliyahu et al., 2015; Sone and Zoback, 2013) and is therefore preferentially deformed during artificial compression experiments in the laboratory (Sone et al., 2015). Similarly, natural compression of organic pores can reasonably occur in complex tectonic deformation settings. The Wufeng–Longmaxi shale has experienced several episodes (particularly during the Jurassic–Cretaceous and Cenozoic) of tectonic deformation following organic pore generation (Hao et al., 2013). As a result of these tectonic events, the mechanical deformation of organic pores has been widely documented in the Wufeng–Longmaxi shale (Guo et al., 2022; Liu et al., 2020a, 2020b; Wang, 2020). Tectonic deformation altered the organic pore morphology from spherical to elliptical (or even slit-like) shapes with increasing aspect ratios in SEM images (Fig. 10) while compressing the pore volume by varying degrees. This process complicates the relationship between TOC content and porosity (Guo et al., 2022; Liu et al., 2020a, 2020b; Wang, 2020).

The study area is characterized by a series of detachment folds (Figs. 1(b) and 2). We observed the morphology change of organic pores from a circular bubble-like shape to an elongated shape (Fig. 10) and a decrease in porosity from 5.22%–6.44% to 3.57%–4.05% at similar TOC contents (Fig. 8) as the syncline

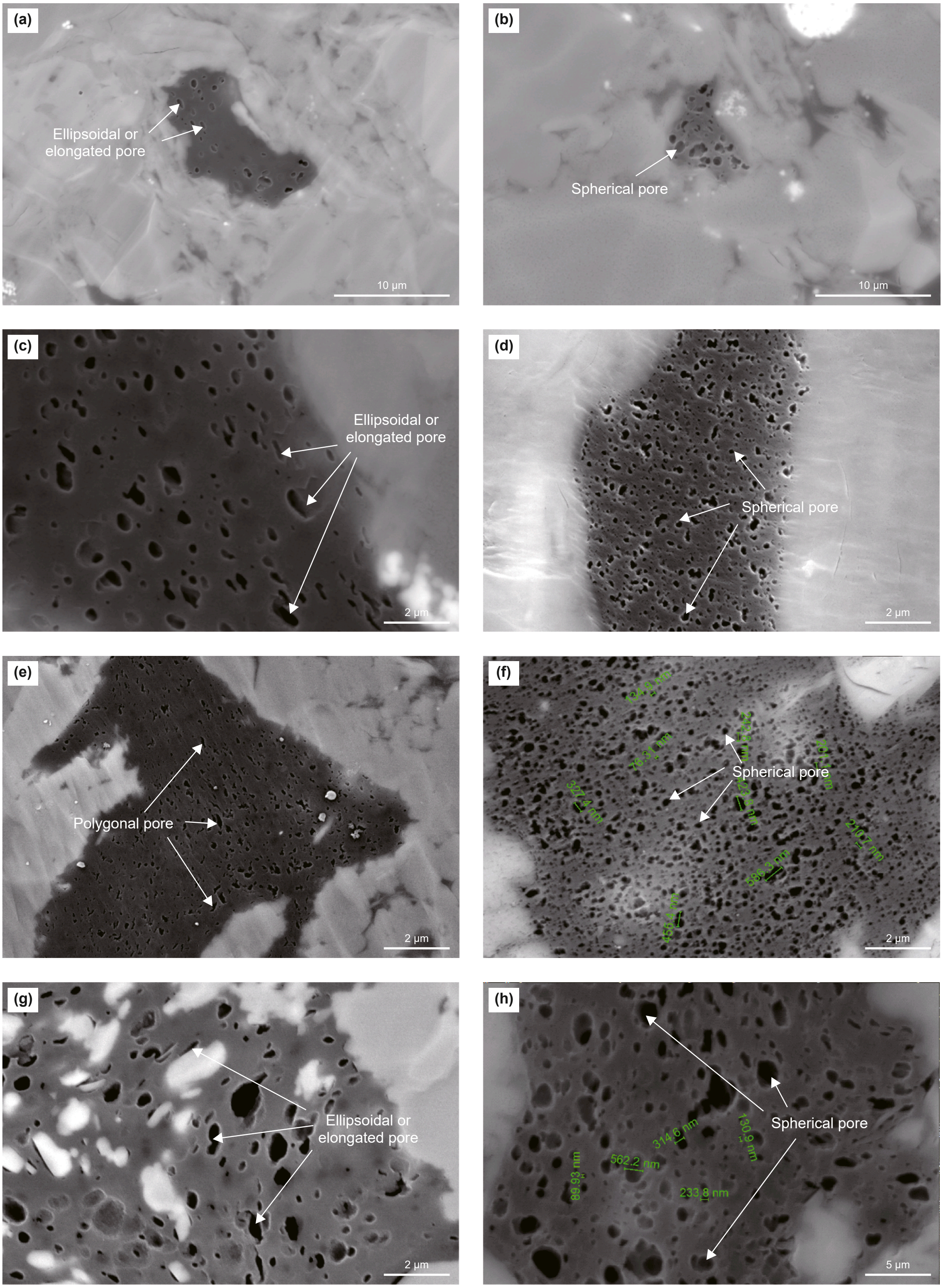

Fig. 10. Scanning electron microscopy (SEM) images depicting the organic pore morphology in Wufeng–Longmaxi shale samples obtained from various depths: **(a)** ZX07 at 4376.68 m, **(b)** ZX07 at 4376.68 m, **(c)** ZX03 at 4108.15 m, **(d)** ZX03 at 4081.23 m, **(e)** ZX08 at 4360.86 m, **(f)** ZX08 at 4366.05 m, and **(g)** ZX08 at 4370.8 m.

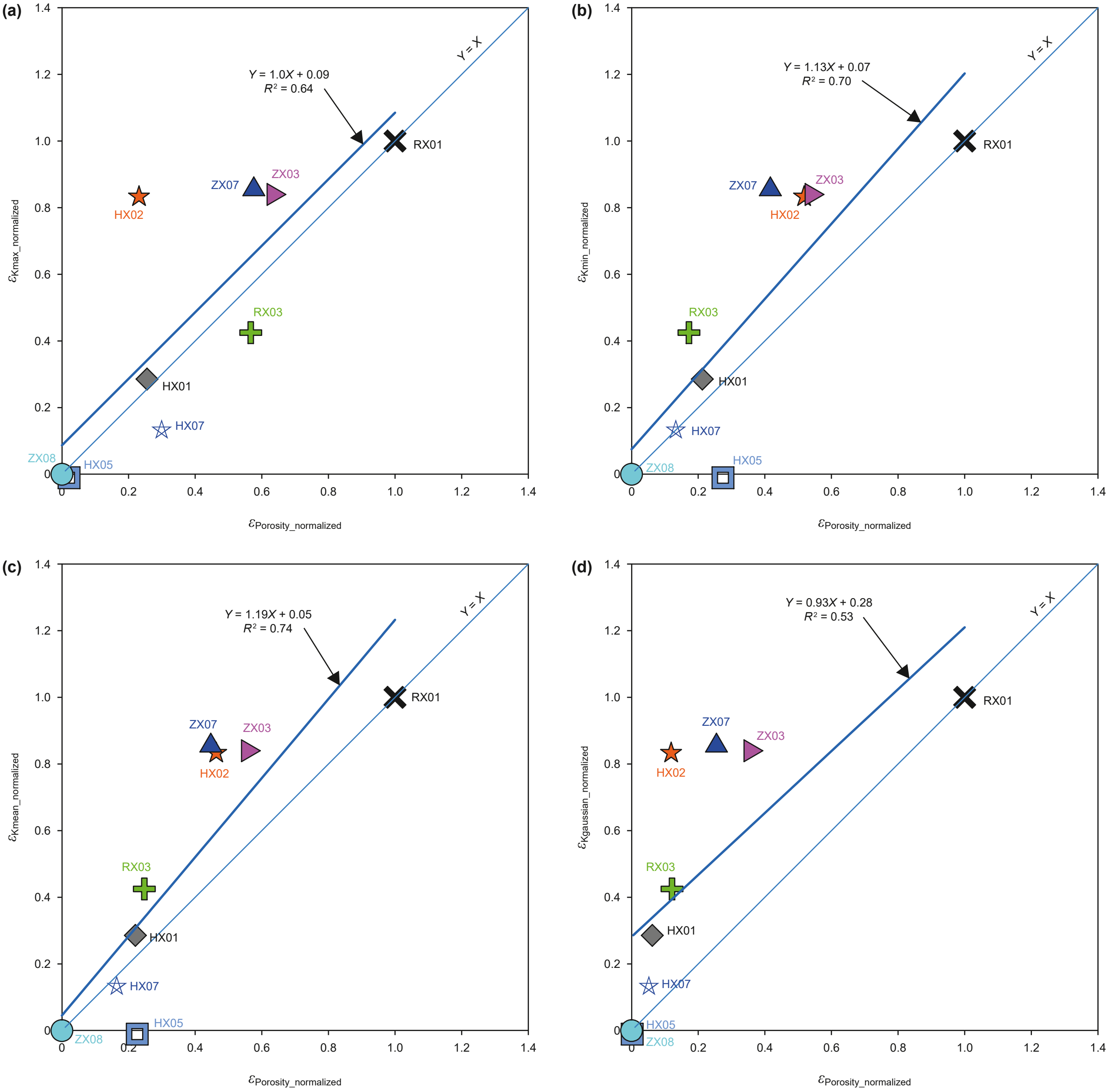

Fig. 11. Comparisons between porosity-based strain ($\varepsilon_{\text{Porosity\_normalized}}$) with **(a)** K_{max}-based ($\varepsilon_{\text{Kmax\_normalized}}$), **(b)** K_{min}-based ($\varepsilon_{\text{Kmin\_normalized}}$), **(c)** K_{mean}-based ($\varepsilon_{\text{Kmean\_normalized}}$), and **(d)** K_{gaussian}-based ($\varepsilon_{\text{Kgaussian\_normalized}}$) strains. All strain values have been normalized to the maximum values observed in borehole RX01.

$|K_{\text{gaussian}}|$ (or $|K_{\text{max}}|$, $|K_{\text{min}}|$, $|K_{\text{mean}}|$) increased (Fig. 9). The observed changes in organic pore morphology and porosity within the syncline structure suggest that the rocks experienced ductile strain. This strain accumulation likely results from more intense folding in synclines with high curvature values (e.g., $|K_{\text{gaussian}}|$, $|K_{\text{max}}|$, $|K_{\text{min}}|$, and $|K_{\text{mean}}|$). Therefore, we infer that the porosity reduction or collapse, induced by ductile strain from syncline bending, was the primary factor driving porosity variations across the different structural settings in the Wufeng–Longmaxi shale.

5.2. Ductile strain of syncline bending

The ductile strain produced by the syncline bending of the Wufeng–Longmaxi shale can be modeled as follows:

$$\Delta\varepsilon_i = h/(2\Delta r_i) = \Delta K_i \times h/2 = (K_i - K_0) \times h/2 \tag{4}$$

where ε_i, r_i, K_i, and h are the syncline bending strain, radius of syncline bending curvature (at deformation step i), curvature parameter (at deformation step i), and thickness (assumed to be a constant) of the Wufeng–Longmaxi shale, respectively (Roberts, 2001). Otherwise, assuming that porosity reduction/collapse was the primary contributor to the syncline bending strain in the Wufeng–Longmaxi shale,

$$\varepsilon_i = (V_0 - V)/V_0 = 1 - V/V_0 = 1 - (1 - P_0)/(1 - P) \tag{5}$$

where V_0 and V denote the rock volume before and after syncline bending, respectively; P_0 and P_i denote the porosities before and after the syncline bending, respectively (Dunham and Crider, 2012; Keating and Fischer, 2008; Moore et al., 2011). As shown in Fig. 9,

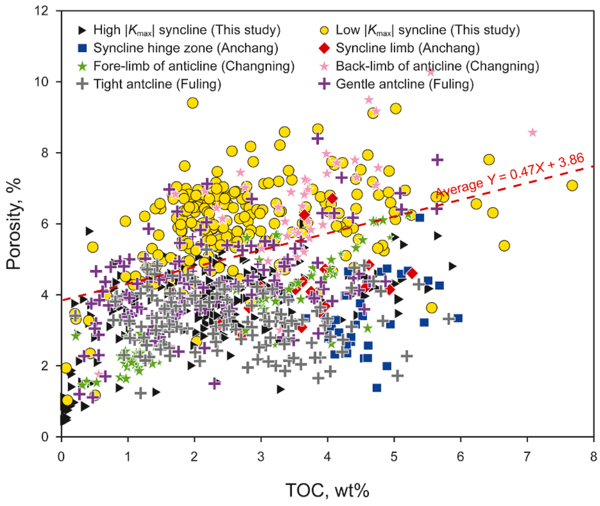

Fig. 12. Porosity comparison of the Wufeng-Longmaxi shale between syncline samples in this study with anticline samples in the Changning and Fuling areas, as well as syncline samples in the Anchang area (Guo et al., 2022; Liu et al., 2020a, 2020b).

borehole ZX08, which has the lowest strain as indicated by lowest $|K_{gaussian}|$ (or $|K_{max}|$, $|K_{min}|$, $|K_{mean}|$), was assumed to represent the initial step of syncline bending (i.e., $K_{max\_0} = 0.97 \times 10^{-7}$ m^{-1}, $K_{min\_0} = -0.13 \times 10^{-4}$ m^{-1}, $K_{mean\_0} = -0.58 \times 10^{-5}$ m^{-1}, $K_{guassian\_0} = -0.12 \times 10^{-10}$ m^{-2}, and $P_0 = 6.44\%$) (Fig. 9, Table 1).

To enable a direct comparison, we normalized Eqs. (4) and (5) using the maximum values of each respective strain measure, as observed in the borehole RX01 data. Despite normalization, curvature-based and porosity-based strains deviate from the $Y = X$ line (Fig. 11), likely reflecting multiscale interactions between macroscopic synclinal strain and microscopic pore deformation, or other porosity-control mechanisms. Nevertheless, widespread linear positive correlations are observed between the curvature- and porosity-based strain (Fig. 11). This confirms that the pore-scale ductile strain dominates the syncline bending of the Wufeng-Longmaxi shale in the study area. Notably, the K_{max}-based strain aligns more closely with the porosity-based strain (Fig. 11(a)), potentially because K_{max} is more sensitive to geological stress and strain, as suggested by Roberts (2001).

Furthermore, the comparison of the syncline bending data with the previously reported anticline bending data (Guo et al., 2022; Liu et al., 2020a, 2020b) (Fig. 12) indicates that there is no significant difference in the extents of ductile strain between the syncline and anticline deformation of the Wufeng-Longmaxi shale in the detachment folding. A porosity reduction of ~2% may be the maximum ductile strain during detachment folding of the Wufeng-Longmaxi shale (Figs. 8 and 12). Instead, the significantly higher K_{max} observed in the anticline relative to the syncline (Fig. 3) may be attributed to the superposition of brittle deformation (i.e., fractures or faults) on pore-scaled ductile strain (Nabavi and Fossen, 2021; Roberts, 2001).

5.3. Stress-strain response

As mentioned in the previous section, we attribute the variation in shale porosity between boreholes with different syncline curvature to ductile strain heterogeneity during detachment folding of the Wufeng–Longmaxi shale (Figs. 9 and 11). Notably, the ductile strain heterogeneity in the Wufeng–Longmaxi shale can reasonably lead to tectonic stress heterogeneity following Hooke's law (Roberts, 2001):

$$\sigma = E \times \Delta K_i \times h/2 \tag{6}$$

where σ and E are the tectonic stress and the Young's modulus of the rock, respectively. Therefore, the higher $|K_{max}|$ or $|K_{min}|$ in the Wufeng–Longmaxi shale during syncline bending indicates a stronger ductile strain and more intense porosity reduction/collapse, resulting in a higher magnitude of principal stress (e.g., the maximum (σ_1) and minimum (σ_3) principal stresses. As illustrated in Fig. 13, the increases in σ_1 and σ_3 to σ'_1 and σ'_3, respectively, can

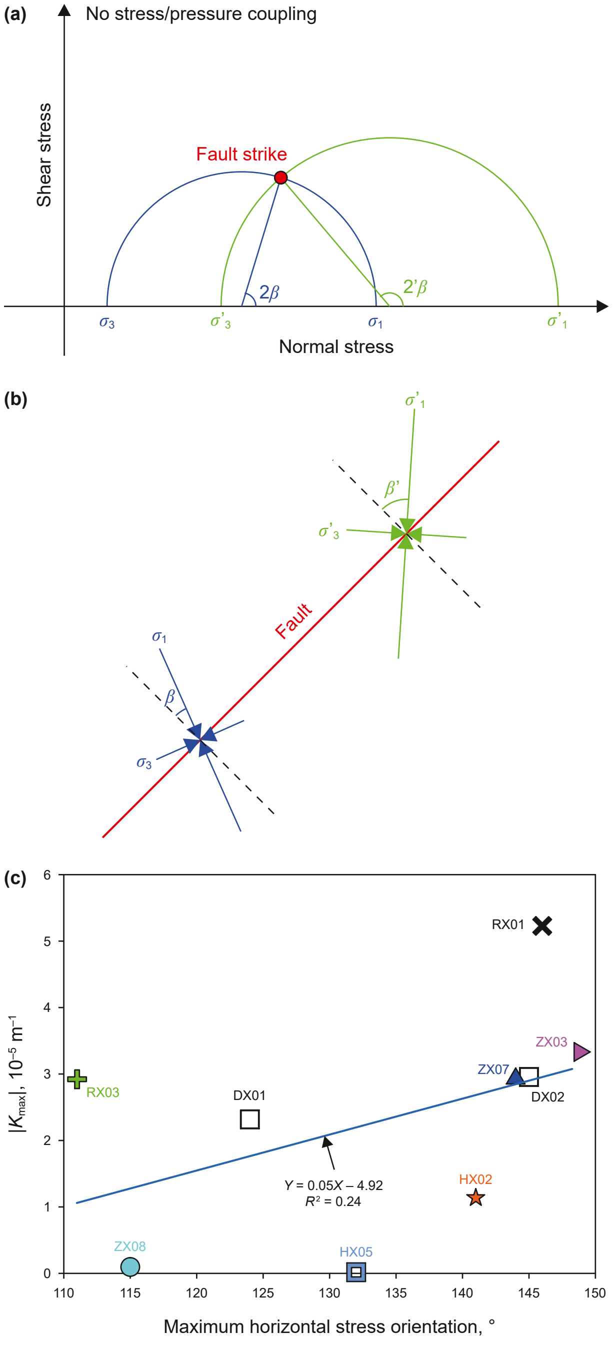

Fig. 13. **(a)** Stress rotation mechanism under conditions without or with the influence of stress/pressure coupling. **(b)** Illustration depicting the outcome of the maximum horizontal stress orientation rotation. **(c)** Cross plot of $|K_{max}|$ with the maximum horizontal principal stress orientations of various boreholes.

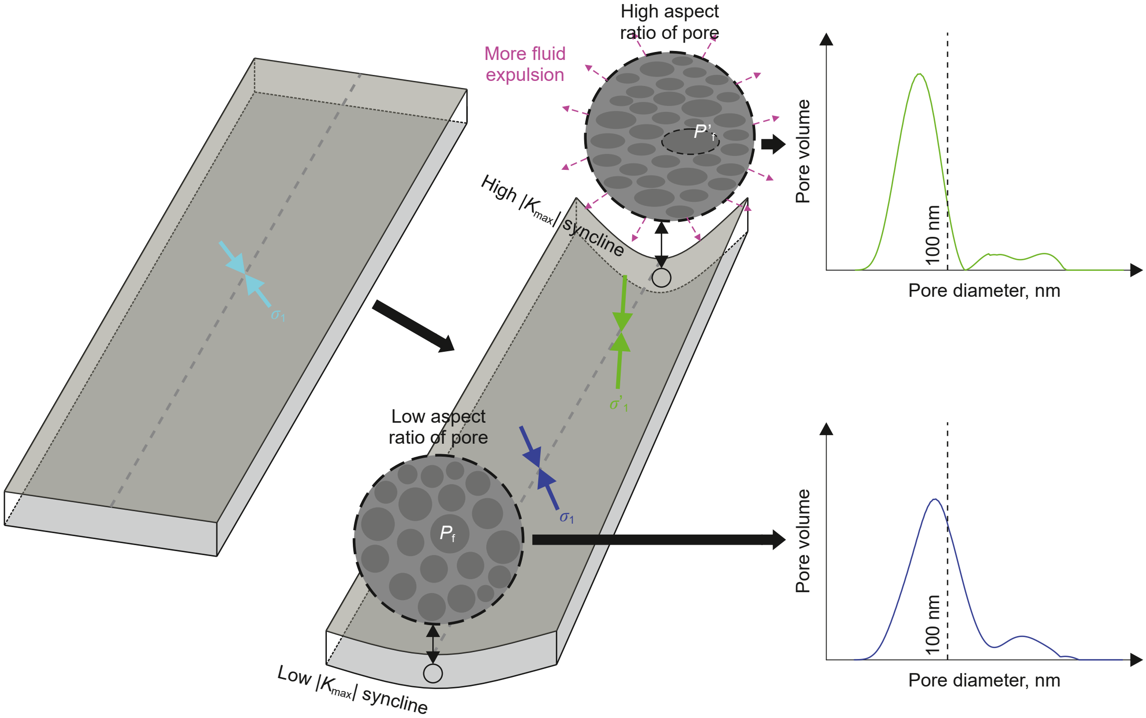

Fig. 14. Correlation model illustrating the relationship between porosity, strain, and stress during syncline bending deformation of the Wufeng–Longmaxi shale in the study area.

also result in a rotation of the principal stress orientation (Hardebeck and Hauksson, 1999; Healy, 2008); for example, the angle (β) between the maximum principal stress orientation and fault normal line increases with rising σ_1 and σ_3 values.

The orientation of the maximum principal stress revealed by drilling-induced tensile fractures and borehole breakouts confirms the clockwise rotation with increasing $|K_{\max}|$ in the Wufeng–Longmaxi shale (Figs. 1(b) and 13). There were approximately 30°–35° and 10° clockwise rotations in the maximum principal stress orientation from ZX08 to ZX07/ZX03 and from HX05 to HX02, respectively. Despite the absence of data on the maximum principal stress orientation in boreholes RX01 and HX01, a clockwise rotation of the principal stress orientation was observed in boreholes DX01 and DX02, which are located within the Linjiang syncline (Figs. 1(b) and 13). A similar rotation of stress orientation induced by stress-strain coupling effect was also reported in the anticlines of the Eastern Fold Belt of the Sichuan Basin (Liu et al., 2021b; Xu et al., 2019).

In summary, a model for coupling pore strain and stress in the Wufeng–Longmaxi shale can be established for the study area as follows (Fig. 14): the variation in bending curvature results in the distinct styles of synclines. The pronounced bending strain in strong-curved synclines can primarily occur as porosity reduction/collapse (Figs. 9 and 11), involving the microscopic ductile strain about the increased pore morphology aspect ratio (Fig. 10) and a decrease in pore size and volume (Figs. 5(c) and (d), 8). The ductile strain heterogeneity in the Wufeng–Longmaxi shale also resulted in tectonic stress heterogeneity even in the same syncline. Stronger bending curvature increased the magnitude of principal stress and induced the clockwise rotations in the maximum principal stress orientation.

Porosity constitutes a critical parameter for predicting shale gas production capacity. Synclines exhibiting weak curvature demonstrate elevated porosity, indicative of favorable reservoir properties and theoretically higher gas production potential. In contrast, strong-curved synclines exhibit significantly reduced shale porosity and diminished dominant pore throat diameters. These alterations constrain gas storage capacity and impede fluid migration pathways, ultimately diminishing production potential. Consequently, shale gas exploration and development strategies must rigorously account for the influence of synclinal ductile strain on porosity and pore architecture. Such assessment enables more accurate identification of reservoir sweet spots and serves as a critical basis for optimizing shale gas resource development.

6. Conclusions

This study reveals considerable variations in pore characteristics with tectonic strain in the Wufeng-Longmaxi shale of the Eastern Fold Belt of the Sichuan Basin. The following conclusions can be obtained:

The Wufeng-Longmaxi shale in the borehole located in the weak curved synclines ($|K_{\text{mean}}| < 0.40 \times 10^{-4}\ \text{m}^{-1}$) exhibits a higher mean porosity of 5.22%–6.44%, with pores that are predominantly spherical. In contrast, the shale in the strong-curved synclines (e.g., $|K_{\text{mean}}| > 0.40 \times 10^{-4}\ \text{m}^{-1}$) displays a reduction of mean porosity to 3.57%–4.05%, accompanied by a transformation of the pore morphology from spherical to more elliptical or slit-like. This change in pore shape was accompanied by a decrease in the dominant pore size, from a range of 1–1000 nm in the weak-curved synclines to 1–100 nm in the strong-curved synclines. These observations suggest that the collapse of organic matter pores occurs at the microscopic level, owing to the relatively low mechanical strength of the organic matter.

The observed porosity changes are consistent with the ductile strain model of syncline bending, suggesting that the porosity changes are triggered by non-uniform deformation strain during detachment folding. The maximum porosity difference between the weak- and strong-curved synclines is approximately 2%, which may be maximum limit of ductile strain during the fold deformation of the Wufeng-Longmaxi shale in the eastern Sichuan Basin.

The strong ductile strain during syncline bending also resulted in the elevation of horizontal principal stress magnitudes and further induced the 10°–30° clockwise rotation of maximum principal stress orientation in the strongly curved synclines.

CRediT authorship contribution statement

Yi-Ting Qiao: Writing – original draft, Investigation, Formal analysis. **Rui Liu:** Writing – original draft, Investigation, Formal analysis. **Shang Xu:** Writing – review & editing, Methodology, Investigation. **Jun-Wei Pu:** Data Curation, Investigation. **Fang Hao:** Conceptualization, Writing - Review & Editing. **Tong-Tong Luo:** Investigation, Validation. **Ke-Xuan Li:** Methodology, Investigation. **Xiu-Cheng Tan:** Project administration, Resources. **Wei-Ming Chen:** Validation. **Yu-Feng Tang:** Investigation.

Declaration of competing interest

The authors declare that they have no known competing financial interests or personal relationships that could have appeared to influence the work reported in this paper.

Acknowledgments

This research was supported by the National Natural Science Foundation of China (No. 42072184, 41702157) and the Science and Technology Cooperation Project of the CNPC-SWPU Innovation Alliance (No. 2020CX010302).

References

Allshorn, S.L., Dawe, R.A., Grattoni, C.A., 2019. Implication of heterogeneities on core porosity measurements. J. Petrol. Sci. Eng. 174, 486–494. https://doi.org/10.1016/j.petrol.2018.11.045.

Aplin, A.C., Macquaker, J.H.S., 2011. Mudstone diversity: Origin and implications for source, seal, and reservoir properties in petroleum systems. AAPG Bull. 95 (12), 2031–2059. https://doi.org/10.1306/03281110162.

Athy, L.F., 1930. Density, porosity, and compaction of sedimentary rocks. AAPG Bull. 14 (1), 1–24. https://doi.org/10.1306/3d93289e-16b1-11d7-8645000102c1865d.

Bergbauer, S., Pollard, D.D., 2003. How to calculate normal curvatures of sampled geological surfaces. J. Struct. Geol. 25 (2), 277–289. https://doi.org/10.1016/S0191-8141(02)00019-6.

Bjørlykke, K., 2014. Relationships between depositional environments, burial history and rock properties. Some principal aspects of diagenetic process in sedimentary basins. Sediment. Geol. 301, 1–14. https://doi.org/10.1016/j.sedgeo.2013.12.002.

Brandes, C., Tanner, D.C., 2014. Fault-related folding: A review of kinematic models and their application. Earth Sci. Rev. 138, 352–370. https://doi.org/10.1016/j.earscirev.2014.06.008.

Chen, L., Jiang, S., Chen, P., et al., 2021. Relative sea-level changes and organic matter enrichment in the upper ordovician-lower Silurian Wufeng-Longmaxi formations in the Central Yangtze area, China. Mar. Petrol. Geol. 124, 104809. https://doi.org/10.1016/j.marpetgeo.2020.104809.

Cheng, G.X., Wu, C.F., Jiang, B., et al., 2024. Pore structure evolution of organic-rich shale induced by structural deformation based on shale deformation experiments. Energy 306, 132463. https://doi.org/10.1016/j.energy.2024.132463.

Curtis, M.E., Cardott, B.J., Sondergeld, C.H., et al., 2012. Development of organic porosity in the Woodford Shale with increasing thermal maturity. Int. J. Coal Geol. 103 (Suppl. C), 26–31. https://doi.org/10.1016/j.coal.2012.08.004.

Degen, T., Sadki, M., Bron, E., et al., 2014. The highscore suite. Powder Diffr. 29 (S2), 13–18. https://doi.org/10.1017/s0885715614000840.

Dewhurst, D.N., Aplin, A.C., Sarda, J.P., et al., 1998. Compaction-driven evolution of porosity and permeability in natural mudstones: An experimental study. J. Geophys. Res. Solid Earth 103 (B1), 651–661. https://doi.org/10.1029/97jb02540.

Dunham, R.E., Crider, J.G., 2012. Geometric curvature analysis of intersecting kink bands: a new perspective on the 3D geometry of kink folds. J. Struct. Geol. 37, 236–247. https://doi.org/10.1016/j.jsg.2012.01.003.

Eliyahu, M., Emmanuel, S., Day-Stirrat, R.J., et al., 2015. Mechanical properties of organic matter in shales mapped at the nanometer scale. Mar. Petrol. Geol. 59 (Suppl. C), 294–304. https://doi.org/10.1016/j.marpetgeo.2014.09.007.

Feng, W.P., Wang, F.Y., Guan, J., et al., 2018. Geologic structure controls on initial productions of lower Silurian longmaxi shale in South China. Mar. Petrol. Geol. 91, 163–178. https://doi.org/10.1016/j.marpetgeo.2018.01.001.

Gao, T., Liu, R., Xu, L., et al., 2025. Genetic mechanism of low resistance in shale analyzed via triaxial compression tests. Bullet. Geolog. Sci. Tech. 44 (2), 224–237. https://doi.org/10.19509/j.cnki.dzkq.tb20230533 (in Chinese).

Gou, Q.Y., Xu, S., Hao, F., et al., 2021. The effect of tectonic deformation and preservation condition on the shale pore structure using adsorption-based textural quantification and 3D image observation. Energy 219, 119579. https://doi.org/10.1016/j.energy.2020.119579.

Guo, X.C., Liu, R., Xu, S., et al., 2022. Structural deformation of shale pores in the fold-thrust belt: the Wufeng-Longmaxi shale in the Anchang Syncline of Central Yangtze Block. Adv. Geo-Energy Res. 6 (6), 515–530. https://doi.org/10.46690/ager.2022.06.08.

Han, Y.J., Horsfield, B., Wirth, R., et al., 2017. Oil retention and porosity evolution in organic-rich shales. AAPG Bull. 101 (6), 807–827. https://doi.org/10.1306/09221616069.

Hao, F., Zou, H.Y., Lu, Y.C., 2013. Mechanisms of shale gas storage: implications for shale gas exploration in China. AAPG Bull. 97 (8), 1325–1346. https://doi.org/10.1306/02141312091.

Hardebeck, J.L., Hauksson, E., 1999. Role of fluids in faulting inferred from stress field signatures. Science 285 (5425), 236–239. https://doi.org/10.1126/science.285.5425.236.

Healy, D., 2008. Damage patterns, stress rotations and pore fluid pressures in strike-slip fault zones. J. Geophys. Res. Solid Earth 113 (B12), 407. https://doi.org/10.1029/2008JB005655.

Heidbach, O., Rajabi, M., Cui, X.F., et al., 2018. The world stress Map database release 2016: Crustal stress pattern across scales. Tectonophysics 744, 484–498. https://doi.org/10.1016/j.tecto.2018.07.007.

Hu, H.Y., Hao, F., Lin, J.F., et al., 2017. Organic matter-hosted pore system in the Wufeng-Longmaxi (O3w-S11) shale, Jiaoshiba area, Eastern Sichuan Basin, China. Int. J. Coal Geol. 173 (Suppl. C), 40–50. https://doi.org/10.1016/j.coal.2017.02.004.

Keating, D.P., Fischer, M.P., 2008. An experimental evaluation of the curvature-strain relation in fault-related folds. AAPG Bull. 92 (7), 869–884. https://doi.org/10.1306/03060807111.

Ko, L.T., Ruppel, S.C., Loucks, R.G., et al., 2018. Pore-types and pore-network evolution in Upper Devonian-Lower Mississippian Woodford and Mississippian Barnett mudstones: Insights from laboratory thermal maturation and organic petrology. Int. J. Coal Geol. 190, 3–28. https://doi.org/10.1016/j.coal.2017.10.001.

Laurich, B., Urai, J.L., Desbois, G., et al., 2014. Microstructural evolution of an incipient fault zone in Opalinus Clay: Insights from an optical and electron microscopic study of ion-beam polished samples from the Main Fault in the Mt-Terri underground Research Laboratory. J. Struct. Geol. 67, 107–128. https://doi.org/10.1016/j.jsg.2014.07.014.

Li, S.J., Li, Y.Q., He, Z.L., et al., 2020. Differential deformation on two sides of Qiyueshan Fault along the eastern margin of Sichuan Basin, China, and its influence on shale gas preservation. Mar. Petrol. Geol. 121, 104602. https://doi.org/10.1016/j.marpetgeo.2020.104602.

Li, C.X., He, D.F., Lu, G., et al., 2021a. Multiple thrust detachments and their implications for hydrocarbon accumulation in the northeastern Sichuan Basin, Southwestern China. AAPG Bull. 105 (2), 357–390. https://doi.org/10.1306/07272019064.

Li, X.S., Zhu, H.J., Zhang, K.X., et al., 2021b. Pore characteristics and pore structure deformation evolution of ductile deformed shales in the Wufeng-Longmaxi Formation, Southern China. Mar. Petrol. Geol. 127, 104992. https://doi.org/10.1016/j.marpetgeo.2021.104992.

Li, X.Y., Chen, S.B., Wu, J.F., et al., 2024. Dynamic variation of full-scale pore compressibility and heterogeneity in deep shale gas reservoirs: Implications for pore system preservation. Energy Fuels 38 (5), 3880–3899. https://doi.org/10.1021/acs.energyfuels.3c04097.

Liang, M.L., Wang, Z.X., Gao, L., et al., 2017. Evolution of pore structure in gas shale related to structural deformation. Fuel 197, 310–319. https://doi.org/10.1016/j.fuel.2017.02.035.

Liu, Y., Yao, Y.B., Liu, D.M., et al., 2018. Shale pore size classification: An NMR fluid typing method. Mar. Petrol. Geol. 96, 591–601. https://doi.org/10.1016/j.marpetgeo.2018.05.014.

Liu, R., Hao, F., Engelder, T., et al., 2020a. Influence of tectonic exhumation on porosity of Wufeng–Longmaxi shale in the Fuling gas field of the eastern Sichuan Basin, China. AAPG (Am. Assoc. Pet. Geol.) Bull. 104 (4), 939–959. https://doi.org/10.1306/08161918071.

Liu, R., Zheng, J., Hao, F., et al., 2020b. Variation in pore systems with tectonic stress in the overthrust Wufeng-Longmaxi shale of the southern Sichuan Basin, China. J. Nat. Gas Sci. Eng. 83, 103617. https://doi.org/10.1016/j.jngse.2020.103617.

Liu, R., Jiang, D.C., Zheng, J., et al., 2021a. Stress heterogeneity in the Changning shale-gas field, southern Sichuan Basin: Implications for a hydraulic fracturing strategy. Mar. Petrol. Geol. 132, 105218. https://doi.org/10.1016/j.marpetgeo.2021.105218.

Liu, S.G., Yang, Y., Deng, B., et al., 2021b. Tectonic evolution of the Sichuan Basin, Southwest China. Earth Sci. Rev. 213, 103470. https://doi.org/10.1016/j.earscirev.2020.103470.

Lohr, S.C., Baruch, E.T., Hall, P.A., et al., 2015. Is organic pore development in gas shales influenced by the primary porosity and structure of thermally immature organic matter? Org. Geochem. 87, 119–132. https://doi.org/10.1016/j.orggeochem.2015.07.010.

Lu, Y.B., Hao, F., Lu, Y.C., et al., 2020. Lithofacies and depositional mechanism of the Ordovician-Silurian Wufeng-Longmaxi organic-rich shales in the Upper Yangtze area, Southern China. AAPG Bull. 104 (1), 97–129. https://doi.org/10.1306/04301918099.

Luffel, D.L., Howard, W.E., 1988. Reliability of laboratory measurement of porosity in tight gas sands. SPE Form. Eval. 3 (4), 705–710. https://doi.org/10.2118/16401-PA.

Ma, Y., Ardakani, O.H., Zhong, N.N., et al., 2020. Possible pore structure deformation effects on the shale gas enrichment: An example from the Lower Cambrian shales of the Eastern Upper Yangtze Platform, South China. Int. J. Coal Geol. 217, 103349. https://doi.org/10.1016/j.coal.2019.103349.

Mastalerz, M., Schimmelmann, A., Drobniak, A., et al., 2013. Porosity of Devonian and Mississippian New Albany Shale across a maturation gradient: Insights from organic petrology, gas adsorption, and mercury intrusion. AAPG Bull. 97 (10), 1621–1643. https://doi.org/10.1306/04011312194.

Mitra, S., 2003. A unified kinematic model for the evolution of detachment folds. J. Struct. Geol. 25 (10), 1659–1673. https://doi.org/10.1016/S0191-8141(02)00198-0.

Mondol, N.H., Bjørlykke, K., Jahren, J., et al., 2007. Experimental mechanical compaction of clay mineral aggregates—Changes in physical properties of mudstones during burial. Mar. Petrol. Geol. 24 (5), 289–311. https://doi.org/10.1016/j.marpetgeo.2007.03.006.

Moore, G.F., Saffer, D., Studer, M., et al., 2011. Structural restoration of thrusts at the toe of the Nankai Trough accretionary prism off Shikoku Island, Japan: Implications for dewatering processes. G-cubed 12 (5), Q0AD12. https://doi.org/10.1029/2010GC003453.

Morley, C.K., Naghadeh, D.H., 2018. Tectonic compaction shortening in toe region of isolated listric normal fault, North Taranaki Basin, New Zealand. Basin Res. 30 (S1), 424–436. https://doi.org/10.1111/bre.12227.

Nabavi, S.T., Fossen, H., 2021. Fold geometry and folding – A review. Earth Sci. Rev. 222, 103812. https://doi.org/10.1016/j.earscirev.2021.103812.

Olgaard, D.L., Nuesch, R., Urai, J.L., 1995. Consolidation of water saturated shales at great depth under drained condition. In: Paper Presented at the 8th International Society Mechanics and Rock Engineering Congress, September 25–29, Tokyo, Japan, No. ISRM-8CONGRESS-1995-058.

Ran, B., Yang, X.R., Qi, S.Y., et al., 2025. Evolution of continental weathering and upwelling in early Silurian and the implications for the organic matter accumulations in the black shales of Longmaxi Formation in the Upper Yangtze Block of South China. Bullet. Geolog. Sci. Tech. 44 (4), 217–232. https://doi.org/10.19509/j.cnki.dzkq.tb20240678 (in Chinses).

Roberts, A., 2001. Curvature attributes and their application to 3D interpreted horizons. First Break 19 (2), 85–100. https://doi.org/10.1046/j.0263-5046.2001.00142.x.

Saito, S., Goldberg, D., 2001. Compaction and dewatering processes of the oceanic sediments in the Costa Rica and Barbados subduction zones: Estimates from in situ physical property measurements. Earth Planet Sci. Lett. 191 (3), 283–293. https://doi.org/10.1016/S0012-821X(01)00403-4.

Screaton, E., Saffer, D., Henry, P., et al., 2002. Porosity loss within the underthrust sediments of the Nankai accretionary complex: Implications for overpressures. Geology 30 (1), 19–22. https://doi.org/10.1130/0091-7613(2002)030<0019:Plwtus>2.0.Co;2.

Shi, S.Y., Wang, Y.P., Guo, H.J., et al., 2021. Variations in pore structure of marine shale from the same horizon of the Longmaxi Formation with changing position in a small-scale anticline: Implications for the influence of structural deformation. Mar. Petrol. Geol. 124, 104837. https://doi.org/10.1016/j.marpetgeo.2020.104837.

Sone, H., Zoback, M.D., 2013. Mechanical properties of shale-gas reservoir rocks - part 1: Static and dynamic elastic properties and anisotropy. Geophysics 78 (5), D378–D389. https://doi.org/10.1190/geo2013-0050.1.

Sone, H., Morales, L.F., Dresen, G., 2015. Microscopic observations of shale deformation from in-situ deformation experiments conducted under a scanning electron microscope. In: The 49th ARMA US Rock Mechanics/Geomechanics Symposium, 28 June–1 July, San Francisco, California, ARMA, No. ARMA-2015-027.

Tong, Y.B., Sun, Y.J., Wu, Z.H., et al., 2018. Passive crustal clockwise rotational deformation of the Sichuan Basin since the Miocene and its relationship with the tectonic evolution of the fault systems on the eastern edge of the Tibetan Plateau. GSA Bulletin 131 (1–2), 175–190. https://doi.org/10.1130/B31965.1.

Wang, E.C., Meng, K., Su, Z., et al., 2014. Block rotation: Tectonic response of the Sichuan basin to the southeastward growth of the Tibetan Plateau along the Xianshuihe-Xiaojiang fault. Tectonics 33 (5), 686–718. https://doi.org/10.1002/2013TC003337.

Wang, G.C., 2020. Deformation of organic matter and its effect on pores in mud rocks. AAPG Bull. 104 (1), 21–36. https://doi.org/10.1306/04241918098.

Xu, S., Liu, R., Hao, F., et al., 2019. Complex rotation of maximum horizontal stress in the Wufeng-Longmaxi Shale on the eastern margin of the Sichuan Basin, China: Implications for predicting natural fractures. Mar. Petrol. Geol. 109 (11), 519–529. https://doi.org/10.1016/j.marpetgeo.2019.06.008.

Yan, D.P., Zhou, M.F., Song, H.L., et al., 2003. Origin and tectonic significance of a Mesozoic multi-layer over-thrust system within the Yangtze Block (South China). Tectonophysics 361 (3–4), 239–254. https://doi.org/10.1016/s0040-1951(02)00646-7.

Yang, W., Wang, Y.H., Du, W., et al., 2022. Behavior of organic matter-hosted pores within shale gas reservoirs in response to differential tectonic deformation: Potential mechanisms and innovative conceptual models. J. Nat. Gas Sci. Eng. 102, 104571. https://doi.org/10.1016/j.jngse.2022.104571.

Zhu, H.J., Ju, Y.W., Qi, Y., et al., 2018. Impact of tectonism on pore type and pore structure evolution in organic-rich shale: Implications for gas storage and migration pathways in naturally deformed rocks. Fuel 228, 272–289. https://doi.org/10.1016/j.fuel.2018.04.137.

Zou, C.N., Qiu, Z., Poulton, S.W., et al., 2018. Ocean euxinia and climate change "double whammy" drove the late Ordovician mass extinction. Geology 46 (6), 535–538. https://doi.org/10.1130/G40121.1.